Interaction between trailing edge wake and vortex rings in a Francis turbine at runaway condition: Compressible large eddy simulation

Chirag Trivedi, and Ole Gunnar Dahlhaug

Citation: Physics of Fluids **30**, 075101 (2018); doi: 10.1063/1.5030867
View online: https://doi.org/10.1063/1.5030867
View Table of Contents: http://aip.scitation.org/toc/phf/30/7
Published by the American Institute of Physics

Interaction between trailing edge wake and vortex rings in a Francis turbine at runaway condition: Compressible large eddy simulation

Chirag Trivedi[a] and Ole Gunnar Dahlhaug
Department of Energy and Process Engineering, Faculty of Engineering, NTNU—Norwegian University of Science and Technology, Trondheim, Norway

(Received 26 March 2018; accepted 11 June 2018; published online 2 July 2018)

The present study aims to investigate the unsteady flow phenomenon that produces high energy stochastic fluctuations in a highly skewed blade cascade. A complex structure such as a turbine is operated at runaway speed, where the circumferential velocity is dangerously high, and the energy dissipation is so significant that it takes a toll on the operating life of a machine. Previous studies showed that a large vortical structure changes the spatial location very quickly and interacts with the secondary flow attached to the blade pressure-side. The temporal inception of the rings dissipates the energy of a wide frequency band and induces heavy vibration in the mechanical structure. The focus of the present study is to experimentally measure and numerically characterize the time-dependent inception of vortex rings in the blade cascade. The experimental data are used to verify and validate the numerical results obtained from the large eddy simulation. Flow compressibility is considered to obtain more accurate amplitudes of unsteady pressure pulsations associated with the wave propagation and reflection. The following three aspects are of particular focus: (1) How the wake from a guide vane interacts with the stagnation point of a blade, (2) how vortex rings are developed in a blade cascade, and what are the temporal characteristics, and (3) how the decelerating flow at the runner outlet interacts with the secondary flow in the draft tube. *Published by AIP Publishing.* https://doi.org/10.1063/1.5030867

I. INTRODUCTION

Vortex breakdown and its consequences have been investigated in most engineering structures, starting from a simplified object such as a cylinder[1,2] to the giant tower of a wind turbine.[3] The remarkable features of vortex breakdown have been studied over the years, especially curved surfaces (wings and turbomachinery blades), where gradients of different velocity components play distinct roles during the formation and destruction of vortices.[4–8] To achieve high efficiency and reduce cost, the profiles of turbine blades are complex and highly skewed from the hub to the tip as well as from the leading edge to the trailing edge. The skewed profiles, however, induce a strong vortex shedding, when the turbines are operated under off-design conditions.[9–11] In this paper, one such case of the skewed blade profile has been investigated. Blade profiles of high head hydraulic turbines are extremely skewed and twisted up to 180° from the leading edge to the trailing edge and up to 90° from the hub to the shroud along the chord length, to attain an efficiency of more than 95%. When the turbines are operated at off-design, vortex breakdown from the blade trailing edge hinders the turbine operation.[12] The runaway condition is a consequence of an unexpected event, such as cascade tripping, fault, and out-of-phase synchronization, of a turbine. Although turbines are expected to experience such events only a few times over their lifetime, the resulting damage is so significant that it takes a toll on the operating life of the machine.[13–15] At runaway speed, the circumferential velocity at the blade leading edge is dangerously high, and the available hydraulic energy dissipates on the blades without producing an active power. The high-amplitude pressure fluctuations are inevitable, inducing fatigue in the blades.

In a high head Francis turbine, a gap (vaneless space) between the rotor (runner) and stator (guide vane) is small, and resulting pressure fluctuations, associated with rotor-stator interaction (RSI), are one of the key concerns for both turbine manufacturers and operators. Several cases of turbine failures have been reported, and the majority of these failures pertained to RSI.[16–19] High circumferential velocity at runaway conditions steeply increases the pressure amplitudes in the turbine. Experimental studies showed that the amplitudes can increase up to three times the normal operating condition.[20] The amplitudes corresponded to both deterministic and stochastic frequencies in the turbine. The source of stochastic fluctuations was unsteady vortical flow in the blade channels. Numerical simulations at the runaway condition showed three distinct vortical regions in each channel.[21] A vortical region located near the blade trailing edge, the crown side, was inducing high amplitude stochastic fluctuations. Such fluctuations induce dynamic stresses in the blades and induce fatigue after certain cycles of operation. Studies[22–24] on pump-turbines at runaway conditions have shown a pressure amplitude of a similar nature, especially around the S-shaped region. Xia *et al.*[25] conducted a numerical study on a pump-turbine under runaway conditions. They observed reverse flow from the hub to the shroud, as the trajectory comes forward and backward within an S-shaped region. Experiments carried out by Hasmatuchi *et al.*[26] and Botero *et al.*[27] showed that the effect

[a]Email: chirag.trivedi@ntnu.no

of the rotating stall is prominent in a pump-turbine at the runaway speed. The stalled region rotates in the same direction as the impeller but with 50%–70% of the rotational speed of the impeller. Although there is a similarity between the Francis runner and pump-turbine impeller, a rotating stall is rarely observed in the Francis runner, but the vortical flow structure in the blade channels is identical.[28,29]

Most numerical studies at runaway conditions are performed using a Reynolds-averaged Navier-Stokes (RANS)-based scale-adaptive simulation (SAS) approach.[30] The SAS showed difficulties at runaway conditions, especially to capture the stochastic fluctuations and the correct amplitudes.[31] At runaway speed, the flow condition is challenging due to the strong separation and the presence of a swirl. Due to the RANS-based formulation, the SAS has certain limitations[32] in regard to the resolution of turbulent scales near the wall. Large eddy simulation (LES)[33–35] has shown remarkable performance over the RANS models[36–39] and the SAS.[40] Understanding of the complex flow field and the characteristic frequencies is vital for the safe and reliable design of turbine blading. The LES is expected to be able to answer the research questions associated with the challenging flow conditions present in the turbine blade cascade. Previous work[35,41] showed the benefit of compressible flow simulations over the incompressible flow in the Francis turbine. The flow compressibility accounts for the effect of pressure waves and reflection from the guide vanes and the draft tube similar to the actual turbine.[42] This allows better prediction of amplitudes pertained to deterministic and stochastic frequencies in the turbine. The present study focuses on the following specific aspects of the runaway condition: (1) How the wake from a guide vane interacts with the stagnation point of a blade, (2) how the vortical flow is developed in a blade passage, and (3) how a draft tube flow interacts with a reverse flow in the blade passage.

II. FRANCIS TURBINE

A. Experimental setup

The state-of-the-art facility available at NTNU—Norwegian University of Science and Technology—is used to conduct detailed measurements. The test rig is a reduced scale (1:5.1) model of a prototype Francis turbine operating in Norway. The model turbine includes 14 stay vanes integrated into the spiral casing, 28 guide vanes, a runner with 15 blades and 15 splitters, and a draft tube. The runner inlet and outlet diameters are 0.63 and 0.347 m, respectively. The test facility is used to conduct industrial model tests according to IEC 60193[43] and is equipped with important sensors to acquire data on the head, flow rate, torque, power, water temperature, and rotational speed. Eight new sensors were flush-mounted to acquire unsteady pressure fluctuations from different locations in the turbine, as seen in Fig. 1. Two sensors (V_1 and V_2) were located on the facing place toward the vaneless space, close to the trailing edge of the guide vane. Four sensors (R_1, R_2, R_3, and R_4) were on the runner crown. A slip-ring mechanism was used to transmit the pressure data from the runner. Two sensors, D_1 and D_2, were positioned 0.126 m downstream from the runner outlet in the draft tube and 180° circumferentially apart. The pressure data were acquired at a sampling rate of 5 kHz, which was ten times the maximum expected frequency in the turbine. The calibration of all the instruments and pressure sensors was carried out before the measurements were performed. The total uncertainty ($\hat{e}_t$) is ±0.21%, including systematic ($\hat{e}_s$) and random ($\hat{e}_r$) uncertainties, at the best efficiency point (BEP). The uncertainties of the pressure sensors situated in the vaneless space, runner, and draft tube were measured as ±0.12%, ±0.26%, and ±0.14%, respectively,

$$\hat{e}_t = \pm\sqrt{\hat{e}_s^2 + \hat{e}_r^2}. \quad (1)$$

B. Numerical setup

A complete turbine similar to the laboratory model, including inlet conduits (length = 5 m and diameter = 0.35 m), labyrinth seals, and tanks (length = 4 m and diameter = 2.5 m) connected to the draft tube outlet, was considered for the numerical study. The numerical model was divided into seven domains as follows: (1) an inlet conduit, a spiral casing, and 14 stay vanes; (2) a stay ring with 28 guide vanes; (3) a runner with 15 blades and 15 splitters; (4) a draft tube;

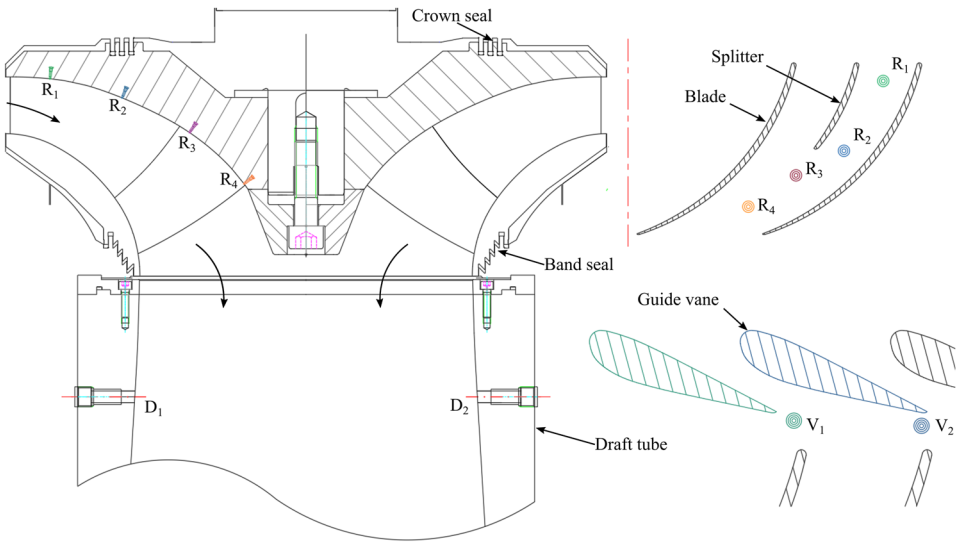

FIG. 1. Locations of the pressure sensors in the turbine. Sensors R_1, R_2, R_3, and R_4 are in the runner; sensors V_1 and V_2 are in the vaneless space; and sensors D_1 and D_2 are in the draft tube.

TABLE I. Range of parameters of the investigated Francis turbine for the present study.

	H (m)	Q (m^3 s^{-1})	T (N m)	n (rps)	Q_{ED}	n_{ED}	η_h	Re	Eu	Fr	St
BEP	12	0.2	616	5.55	0.15	0.18	0.93	2.1×10^6	0.79	6.56	7.42
Runaway	12.07	0.085	12.1	8.53	0.06	0.28	0.19	3.3×10^6	0.33	10.1	28.5

(5) a tank; (6) a crown seal; and (7) a band seal. A hexahedral mesh was created in all the domains, and the total number of nodes was 72×10^6. The first node was placed at 0.001 mm from the no-slip wall to obtain $y^+ \leq 1$, and the subsequent increment was 1.25 times the preceding node. The available supercomputer at the university was used, which required 1.5×10^6 cpu hours to complete the simulations. The rotating and stationary domains were connected through an interface modeling approach, i.e., a multiple reference frame. The frozen rotor and transient rotor-stator interfaces were activated for the steady-state and unsteady analysis, respectively. In the case of a frozen rotor, the pitch is changed but the relative orientation of the rotor and stator across the interface is fixed. The frozen rotor analysis is useful when the circumferential variation of the flow is large relative to the pitch. The transient rotor-stator is used to account for transient interaction of the flow between the stator and the rotor. The interface position is updated each time step, as the relative position of the mesh nodes on each side of the interface changes. This approach requires more memory and computational power as compared to the frozen rotor. A buoyancy model was activated to introduce a gravity effect similar to the actual turbine. Equations (2) and (3) were solved to compute the water density (ρ) and speed of sound (a) during the simulation,[41,44]

$$\rho = \frac{\rho_{ref}}{\left(1 - \frac{p - p_{ref}}{K}\right)} \text{ (kg m}^{-3}\text{)}, \tag{2}$$

$$a = \sqrt{\frac{K\left(1 - \frac{p - p_{ref}}{K}\right)}{\rho_{ref}}} \text{ (ms}^{-1}\text{)}, \tag{3}$$

where ρ_{ref} is the reference density obtained from the measurement, p_{ref} is the reference pressure (101 325 Pa), and K is the modulus of elasticity (2×10^9 Pa) at 20 °C water. To attain an acoustic Courant (C_a) number of approximately one, a time step of 10^{-5} s was used,

$$C_a = \max\left(\frac{(v + a)\Delta t}{\Delta x}, \frac{(v - a)\Delta t}{\Delta x}\right), \tag{4}$$

where v is the flow velocity in m s^{-1}, a is the speed of sound in m s^{-1}, Δt is the time step in seconds, and Δx is an average size of a mesh element in meters. Verification of the four mesh types created (9, 18, 36, and 72×10^6 nodes) was conducted using three different techniques as follows: (1) the grid convergence index,[45] (2) the index of resolution quality for large eddy simulations,[46] and (3) Pope's criterion.[47] The fine mesh with 72×10^6 nodes was selected for the final study. The fine mesh has shown a resolved kinetic energy spectrum more than 80% in the turbine. The detailed verification of the numerical model is presented in the Appendix. For numerical simulations, an ANSYS® CFX® parallel distributed coupled solver was used. This solution approach uses a fully implicit discretization of the equations. The CFX uses an element-based finite volume (node-centered approach) method, which first involves discretizing the spatial domain using the mesh.

C. Range of parameters

Table I shows the range of parameters of the investigated turbine at the BEP and runaway conditions. Hydraulic efficiency and net head of the turbine at the BEP are 93% and 12 m, respectively. The volume flow rate to the turbine at the BEP and runaway conditions is 0.2 m^3 s^{-1} and 0.085 m^3 s^{-1}, respectively. The runaway speed is 8.53 rps, which is 1.54 times the rated speed of the turbine. Measurements of the BEP were conducted to ensure the repeatability and uncertainty quantification of the test rig. Therefore, the data analysis at the BEP is not presented in this paper.

Simulations at the runaway condition were performed using the LES approach. The wall-adapting local eddy (WALE) viscosity model was used for resolving the small-scale eddies in the LES. The WALE is designed to return the correct wall-asymptotic-variation of the sub-grid scale (SGS) viscosity and requires no damping function.[48,49] The WALE viscosity model produces almost no artificial viscosity in wall-bounded laminar flows and is capable of reproducing laminar to turbulent transition.[50] The volume flow rate at the runaway condition is very low, and the Reynolds number is low at certain locations in the turbine, where the WALE viscosity model is an appropriate choice.[51,52] A second-order backward Euler scheme for the temporal discretization and a bounded central-difference scheme for the advection were activated. The convergence criteria for mass and momentum residuals (root-mean-square) were set to 10^{-5}. The selected time step was 10^{-6} s, which is equivalent to 36 000 time steps per rotation of the runner. The total time was equivalent to 10 revolutions of the runner (360 000 time steps). The LES required approximately 3 revolutions to attain a time-average quantity and to resolve the turbulent scales properly. Data of the remaining 7 revolutions are investigated and presented in this paper.

III. RESULTS AND DISCUSSIONS

A. Wake inception behind a guide vane

Two sensors (V_1 and V_2) were mounted in the vaneless space to investigate the vortex shedding from the guide vane, and the numerical monitoring points were created at the same locations. Figure 2 shows the power spectral density of the pressure data at the V_1 location, which is close to the trailing edge of the guide vane in the wake region. Acquired pressure

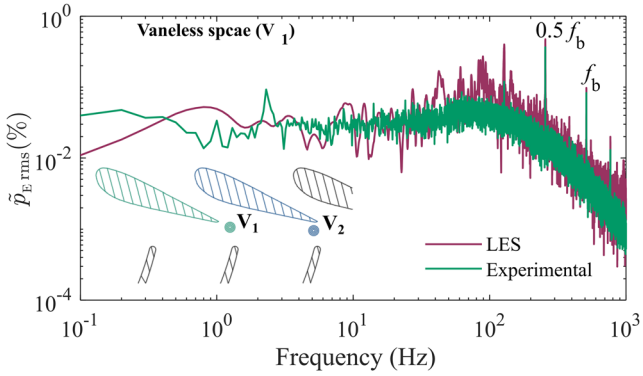

FIG. 2. Power spectra of unsteady pressure fluctuations observed in the vaneless space (V_1).

fluctuations are normalized using Eqs. (5) and (6), where $\tilde{p}(t)$ is the acquired unsteady pressure in Pa, $\bar{p}(t)$ is the time-average pressure at that location in Pa, ρ is the water density at BEP in kg m^{-3}, E is the specific hydraulic energy in J kg^{-1} at BEP, and $\tilde{p}_E$ is the pressure fluctuation factor. High amplitude spikes are the frequencies of the rotor-stator interaction, i.e., a blade-passing frequency (f_b) of 255.7 Hz and harmonics of 127.8, 383.5, and 511.4 Hz,

$$\tilde{p}_E = \frac{\tilde{p}(t) - \bar{p}(t)}{(\rho \cdot E)_{BEP}}, \tag{5}$$

$$\tilde{p}_{E\,rms} = \frac{\tilde{p}_E}{\sqrt{2}}, \tag{6}$$

$$f_b = n_R \cdot z_b\,(\text{Hz}), \tag{7}$$

where n_R is the runaway speed and z_b is the number of blades including splitters. Unlike standard RANS models,[21] the LES has resolved the turbulent spectrum very well, especially stochastic fluctuations of a wide frequency range similar to the experimental range. The stochastic fluctuations correspond to flow separation from the pressure-side of the guide vane and unsteady vortex shedding from the trailing edge. Since the runner was rotating at constant speed, fluctuations associated with the flow separation from the guide vane and the blade position relative to that guide vane have the periodic nature of a wide frequency band. The periodic fluctuations have a wide range of frequencies unlike the characteristic frequencies of rotor-stator interaction. Due to the cascade arrangement of the guide vanes, the flow area in the vaneless space changes from one guide vane to another. Hence, the size of the stagnation point around the blade leading edge and the profile of the wake behind the guide vane vary periodically.

Three numerical points were created in the wake region to investigate velocity fluctuations. Figure 3 shows velocity fluctuations in the wake region with respect to time (t) and the runner angular rotation (θ). Dimensionless velocity (v^*) is computed using the following equation:[53]

$$v^* = \frac{|v|}{v_c}, \tag{8}$$

where $|v| = \sqrt{v_a^2 + v_r^2 + v_\omega^2}$ and $v_c = \sqrt{2 \cdot g \cdot H}$; v_a, v_r, and v_ω are the axial, radial, and circumferential velocities in m s^{-1}, respectively; H is the net head of the turbine in m. High amplitude fluctuations correspond to a point p_3, which is at a distance of 3% of the guide vane chord (c) from the trailing edge along the wake, and the frequency of fluctuations is 656 Hz, which agrees with the vortex shedding frequency computed using Eq. (9),[54] where B = 149 for a trailing edge profile similar to the existing guide vanes, v is the velocity in m s^{-1}, and L is the thickness before the trailing edge in mm. The Strouhal number (St) is 0.22, where f = 656 Hz, L = 2.2 mm, and v = 6.4 m s^{-1}. The other frequency of 767 Hz is obtained, which is the third harmonic of the blade-passing frequency. Dimensionless velocity v^* signifies the magnitude of velocity with respect to the characteristic/theoretical velocity,

$$f = 190 \cdot \frac{B}{100} \cdot \frac{v}{L + 0.56}\,(\text{Hz}), \tag{9}$$

$$St = \frac{f \cdot L}{v}. \tag{10}$$

The velocity distribution in a wake region behind the guide vane at an instantaneous time, i.e., when a blade interacts with the guide vane, is investigated. The velocity in the wake region is almost zero, and small vortices inside the wake are developed and rotate in the clockwise direction. Separating the flow from the guide vane suction-side gives momentum to the vortices in the wake region. A shear layer is established on the round edge of the guide vane. The flow inside the shear layer, separated from the trailing edge, travels in the opposite direction. The layer thickness varies from 0.2% to 1.4% of the chord, depending upon the position of the blade stagnation point relative to the guide vane. Time-dependent interaction of the wake and the blade stagnation point is shown in Fig. 4. Let the reference (start) position of the runner be x/c = 0, where the blade and guide vane are facing each other, and denoted as θ = 0°

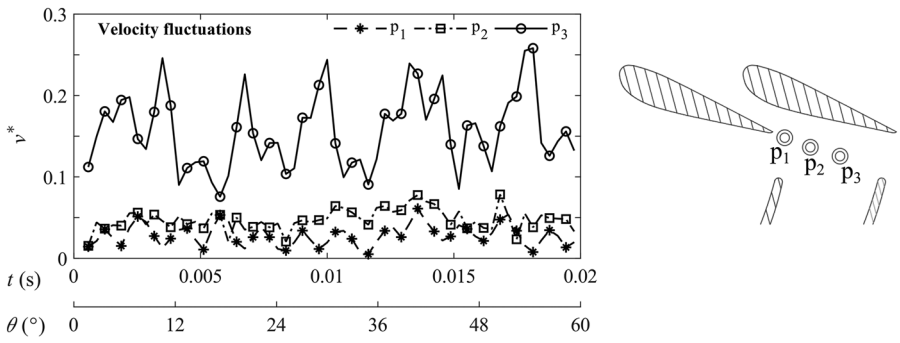

FIG. 3. Time-dependent velocity fluctuations in the wake region behind a guide vane trailing edge. Points p_1, p_2, and p_3 are in the wake region at a distance (x/c) of 0.01, 0.02, and 0.03 from the trailing edge, respectively.

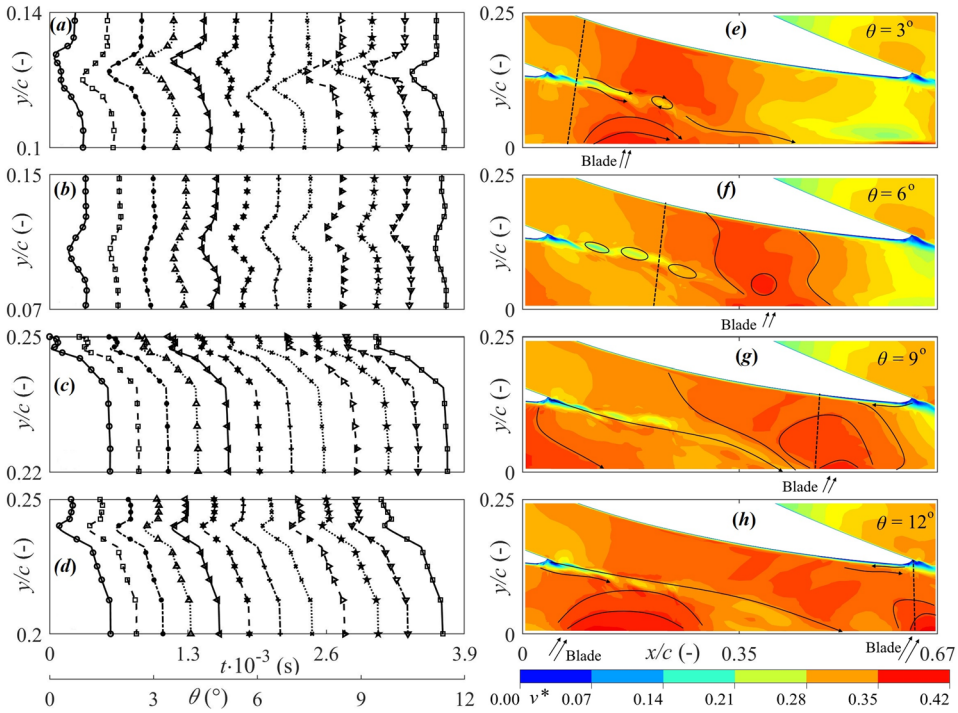

FIG. 4. Time-dependent interaction of the wake behind a guide vane and the stagnation point at the blade leading edge. [(a)–(d)] show the dimensionless velocity (v^*) along a line at $x/c = 0.165$, 0.33, 0.55, and 0.67. [(e)-(h)] show velocity (v^*) contours in the vaneless space and vortex shedding from the trailing edge. $\theta = 0°$ is a reference position, where the blade leading edge and the guide vane trailing edge are facing each other. Dimensionless distance $x/c = 0.67$ is the distance from the trailing edge of one guide vane to another. Dimensionless distance $y/c = 0.25$ is the distance from the runner inlet to the wall of the guide vane. Time (t) 3.9×10^{-3} s corresponds to the 12° angular movement of the runner from the reference position. The scale on the y-axis for [(a)-(d)] is different to emphasize the wake effect.

hereafter. Angular pitch ($s = 360°/z_b$) between two blades is 12° in this turbine. Figures 4(a)–4(d) show the velocity distribution along a line for 0–12° angular movement of a blade from the reference position, and Figs. 4(e)–4(h) show velocity contours for 3°, 6°, 9°, and 12° angular positions of the blade. Figure 4(a) shows velocity in the wake region ($0.1 \le y/c \le 0.14$) along a line at $x/c = 0.165$. The wake profile changes rapidly, which is attributed to the vortex shedding from the pressure- and suction-sides of the guide vane. A vortex from the long wake detaches and spins on the local axis [see Fig. 4(e)]. The detached vortex follows the blade stagnation point, which can be seen in Fig. 4(f). In the meantime, an adverse velocity gradient is established near the guide vane trailing edge ($0.2 \le y/c \le 0.25$) [see Figs. 4(c) and 4(d)]. The shear layer thickness gradually reduces as the blade advances from 6° to 9°. The large size of the stagnation region blocks the flow, and the wake enters the runner. When the blade reaches the 12° position, the stagnation region is reduced due to a small vaneless gap near the trailing edge. Once the blade passes the guide vane, the thickness of the shear layer starts to increase, and more reverse flow near the guide vane wall occurs. The dimensionless maximum velocity (v^*) of 0.42 corresponds to an actual velocity of 9 m s^{-1} in the vaneless space.

Figure 5 shows vorticity and streamline behind a guide vane at time instants of 0°, 3°, 6°, and 9° angular positions of the blade. Inception of the vortex behind the guide vane can be seen in Fig. 5(a). Further development of the vortex and stretching in the wake region can be seen in Figs. 5(b) and 5(c). The developed vortices interact with the blade stagnation point. At the end of the cycle, the size of the vortex grows, and a new vortex is set up at the guide vane trailing edge for another cycle—see Fig. 5(d). To understand more clearly, the time-dependent trajectory of the wake and vortex shedding from the guide vane is established, which is shown in Fig. 6. The trajectory is continuous time-averaged over five revolutions of the runner and for the same blade positions. One snapshot per degree angular movement of the runner was

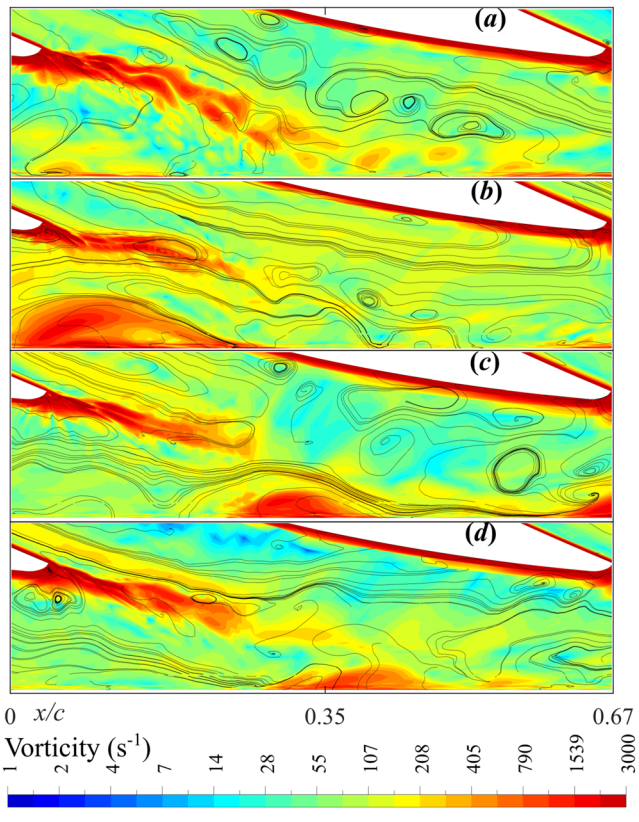

FIG. 5. Vorticity and streamlines behind a guide vane at time instants of (a) 0°, (b) 3°, (c) 6°, and (d) 9° angular positions of the blade.

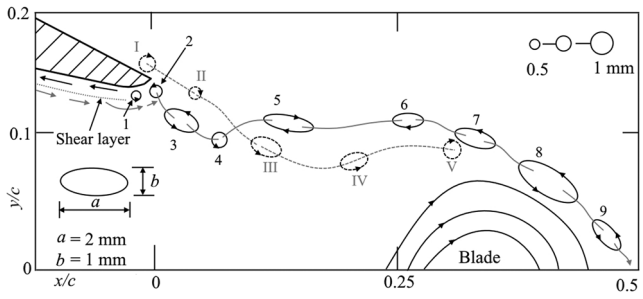

FIG. 6. Trajectory of the wake, vortex inception, and propagation behind a guide vane. The continuous and dashed lines show the vortex inception from suction- and pressure-sides, respectively.

acquired. Data of 0°-12° runner movement were compiled to develop the trajectory. Continuous and dashed lines show the vortex trajectory from the pressure- and suction-sides, respectively. Two vortices are developed, each from the pressure- and suction-sides of the guide vane, and both interact at the trailing edge. When the blade approaches the guide vane trailing edge (i.e., $\theta = 0°$), a small vortex originates in the shear layer, which grows with time and reaches to the trailing edge (see vortex–2). The vortex is further developed and grows along the wake. Then, another vortex from the pressure-side (vortex–I) is developed and travels downstream and gets across the wake region very quickly. Consequently, vortex–4 is pushed upward and changes its path as well as its shape. After a few moments, vortex–V and vortex–7 conjoin and form vortex–8, which is the largest in size and exactly above the blade stagnation point. Later, the vortex shrinks due to the influence of the stagnation region and enters the blade channel. The cycle repeats when the blade reaches the neighboring guide vane trailing edge.

B. Inception of vortex rings

Due to the high rotational speed and low discharge, flow in the runner is more chaotic than flow in the vaneless space. Both circumferential and radial velocities are very high, and the flow angle is very small, which is the perfect recipe for the strong flow separation and inception of vortical flow in the blade cascade. The flow analysis reveals that the separating flow from the blade surface causes reverse (pumping) flow at certain locations in the blade cascade. Flow on the blade pressure-side travels from the inlet to the outlet of the blade channels, whereas flow on the suction-side of the opposite blade travels in the reverse direction, resulting in the development of large vortical structures in the channel. Figure 7 shows the contour of vorticity in the runner at an instantaneous time, i.e., $\theta = 0°$. The vortical flow at certain locations is clearly visible in the blade channels, and the location is dependent on the position of the blade relative to the guide vane. On the blade suction-side, the flow quickly accelerates and detaches from the point where the blade curvature is so steep. On the pressure-side, the flow is circulatory and travels toward the leading edge. The large vortical regions rotate in the counterclockwise direction. To investigate the unsteady fluctuations of the vortical flow, four pressure sensors, R_1, R_2, R_3, and R_4, were positioned in the blade cascade at equal distances. The frequency spectra at these locations and their comparison with the LES are presented in Fig. 8. Figures 8(a)–8(d) show the frequency spectra of the experimental data, and Figs. 8(e)–8(h) show the frequency spectra of the LES. A spike at the RSI frequency (f_{gv}) is clearly visible in the plots. The LES slightly underestimated (1.6%–2%) the amplitudes; however, as compared to the incompressible flow study (12% error),[21] the prediction of amplitudes is more accurate,

$$f_{gv} = n_R \cdot z_{gv}\ (\text{Hz}), \tag{11}$$

where n_R is the runaway speed and z_{gv} is the number of guide vanes in the turbine. The spike at $f^* = 28$ shows the amplitude of the guide vane passing frequency (f_{gv}). In addition to the deterministic frequency of RSI, a wide range of stochastic frequencies are found, especially at R_1 and R_2 locations. The stochastic frequencies are attributed to the unsteady fluctuations from the vortical flow. The moderate effect of artificial reflection of pressure waves (due to the compressibility effect) was observed in LES. This resulted in over-prediction of pressure fluctuations pertained to stochastic frequencies, especially between R_1 and R_2 regions. The effect of flow separation from the blade (splitter) suction-side is high, i.e., between R_1 and R_2 locations. As flow travels from R_1 to R_2, regions of large vortical region break down. This results in change in pressure amplitudes; however, the frequencies remain the same (due to constant rotational speed of the runner and local eddies). At R_3 and R_4 locations, flow from two sides of the splitter interacts, and the vortical regions are split

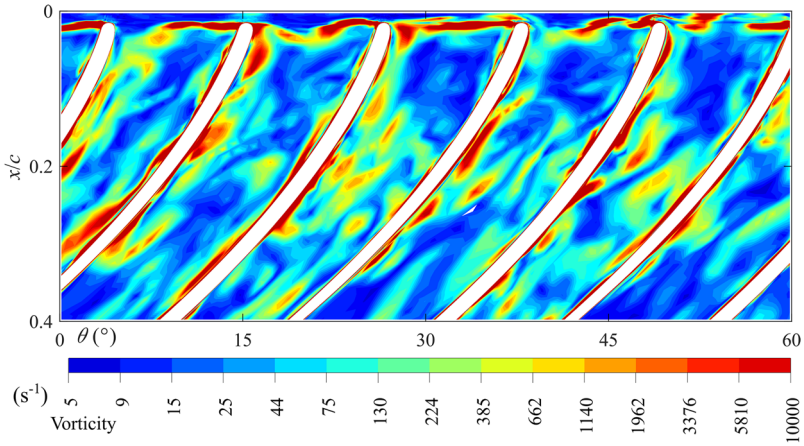

FIG. 7. Contour of vorticity in the runner at an instantaneous time.

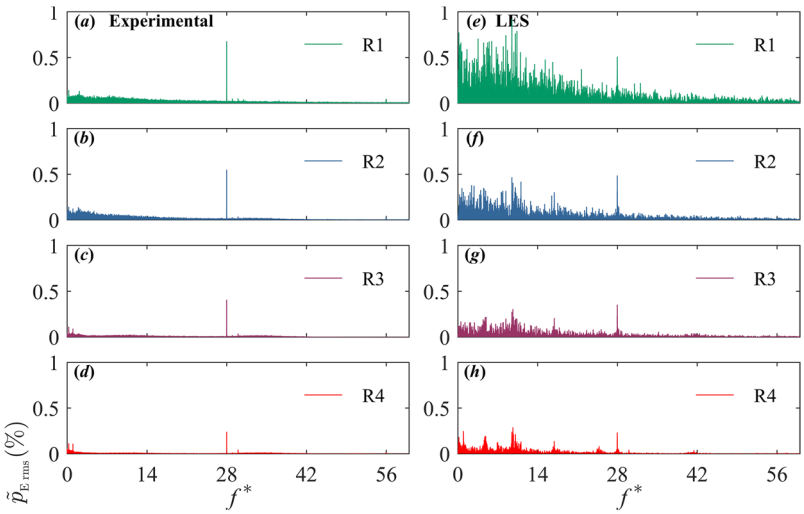

FIG. 8. Frequency spectra of pressure fluctuations in the runner and the comparison with the LES. [(a)–(d)] show the frequency spectra of the experimental data, and [(e)–(h)] show the frequency spectra of the numerical (LES). Amplitudes are normalized by hydraulic energy at the BEP, and the frequency is normalized by the runner rotational speed.

up further. The strength of the vortical region is dependent on the interaction of separated flow from the wall of the blade and the vortex from the guide vane trailing edge. High intensity vortices were found when the blade channel was aligned with the guide vane channel. At this instant in time, vortices from the guide vane trailing edge directly enter into the blade channel.

To study the development of the vortical region from the crown to the band and flow separation on the suction-side, the streamwise velocity distribution along the blade span is investigated, which is shown in Fig. 9(a). The contours of streamwise velocity are at instantaneous time and are presented for 1%, 25%, 50%, 75%, and 99% of the blade span from the crown to the band. At 1% span, the effect of flow separation from the leading edge is small, and near the blade and splitter pressure-side, vortical flow is seen (v_{st} = −9 m s^{-1}). The magnitude of the streamwise velocity reduces toward the mid-span. The intensity of flow separation from the blade/splitter suction-side increases, and the maximum (v_{st} = 14 m s^{-1}) separation can be seen at 75% span. The separated flow integrates with the reverse flow on the splitter pressure-side and constitutes a large vortical zone between 75% and 99% span. Near 99% of the blade span, the effect of reverse flow is very small due to the steep curvature of the runner band and the influence of the boundary layer. Further, how inception of vortical flow affects the blade loading is shown in Figs. 9(b) and 9(c). The factor of pressure loading ($\tilde{p}_E$) on one of the blades for 1%, 50%, and 99% span is shown. Two stagnation points are found on both sides of the leading edge. On the pressure-side, the spike is small compared to the suction-side at $\tilde{p}_E$ = 2.4, and the blade loading is quite different at all three spans. The blades have a positive leaning, toward runner rotation, which has influence on pressure distribution, especially around the leading edge. The effect of the vortical region on the blade loading can be seen for different blade positions. The spike at the leading edge gradually increases as the blade advances from 0° (reference) to 9°, and the maximum value of $\tilde{p}_E$ is obtained between 6° and 9°, where the stagnation region is large. Vortex shedding from the guide vanes directly approaches the leading edge at the 9° blade position. The fluctuating blade loading from x/c = 0.2 to 0.5 indicates the increasing effect of flow separation and the formation of the vortical region. More interestingly, the pressure on the suction-side is higher than that on the pressure-side of the blade. A very small portion of the blade actually

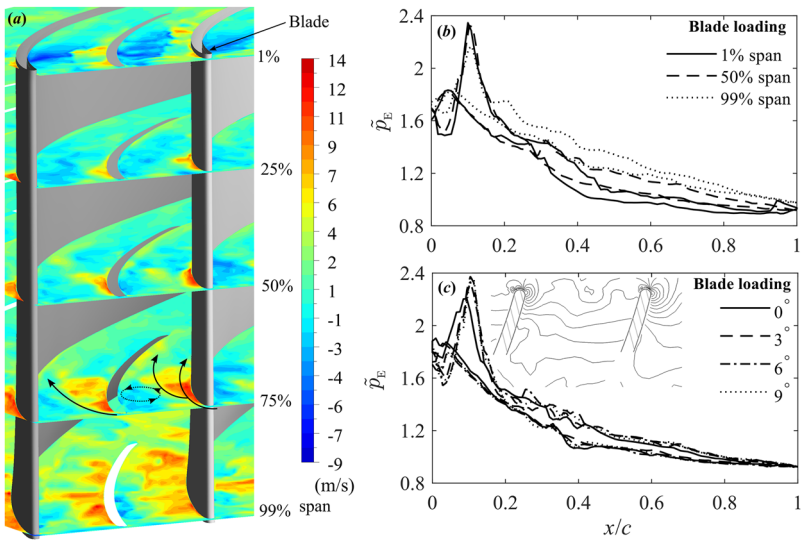

FIG. 9. (a) Streamwise velocity contours (instantaneous time) at 1%, 25%, 50%, 75%, and 99% of the blade span from the crown, (b) blade loading at 1%, 50%, and 99% of the blade span, and (c) blade loading at 50% of the blade span for 0°, 3°, 6°, and 9° angular positions of the blade.

produces the positive torque, which is utilized to overcome the losses (bearing and disc friction) at runaway speed.

Figure 10 shows the inception of vortex rings in the blade cascade and interaction with the wake from the guide vane. The meridional view of the blade cascade is shown in Fig. 10(b). The dimensionless span of zero and one indicates the band and the crown, respectively. The dimensionless streamwise length (x/c) of zero and one indicates the blade leading edge and trailing edges, respectively. A total of 11 vortical regions are identified in the cascade: seven (w_1–w_7) of them are oriented in the axial direction, shown in Fig. 10(a), and the remaining five regions (w_8–w_{11}) are in the circumferential direction, shown in Fig. 10(b). The vortical structure is time-averaged over five exact rotations of the runner, i.e., 0.6 s. The vortical regions, especially those that are axially oriented, follow a distinct path in the blade cascade from the point of inception. Some of the regions grow very quickly along the travel path and interact with the secondary flow. Vortical regions w_1 and w_2 interact with each other when the adjacent blade (blade–2 for this case) is facing the guide vane and, later, the region breaks down. Flow unsteadiness around the vortical regions w_1 and w_2 is evident in terms of stochastic fluctuations around R_1 and R_2 locations in Fig. 8; hence, this can be comparable to the realistic flow in the turbine. Similarly, vortical region w_4 grows to the extent where 95% of the cross-sectional area around w_4 is blocked for a certain time. Another blockade is found near the blade trailing edge, where the circulatory pumping flow and separation from the blade–1 suction-side are dominant. Vortical regions w_8 and w_9 are developed from the adverse pressure gradient on the band and the crown at the inlet, and corner vortices due to flow separation from the blade leading edge junctions to the band and the crown. Another vortical region, w_{11}, is associated with region w_5. The flow field at the blade trailing edge is strongly influenced by the draft tube flow field. The location of w_{11} changes from the suction-side of blade–1 to the pressure-side of blade–2, which is dependent on the blockade created in the blade channel by vortical region w_4. Streamwise velocity fluctuations in the blade channel are shown in Fig. 10(c). The streamwise velocity is normalized by tangential velocity

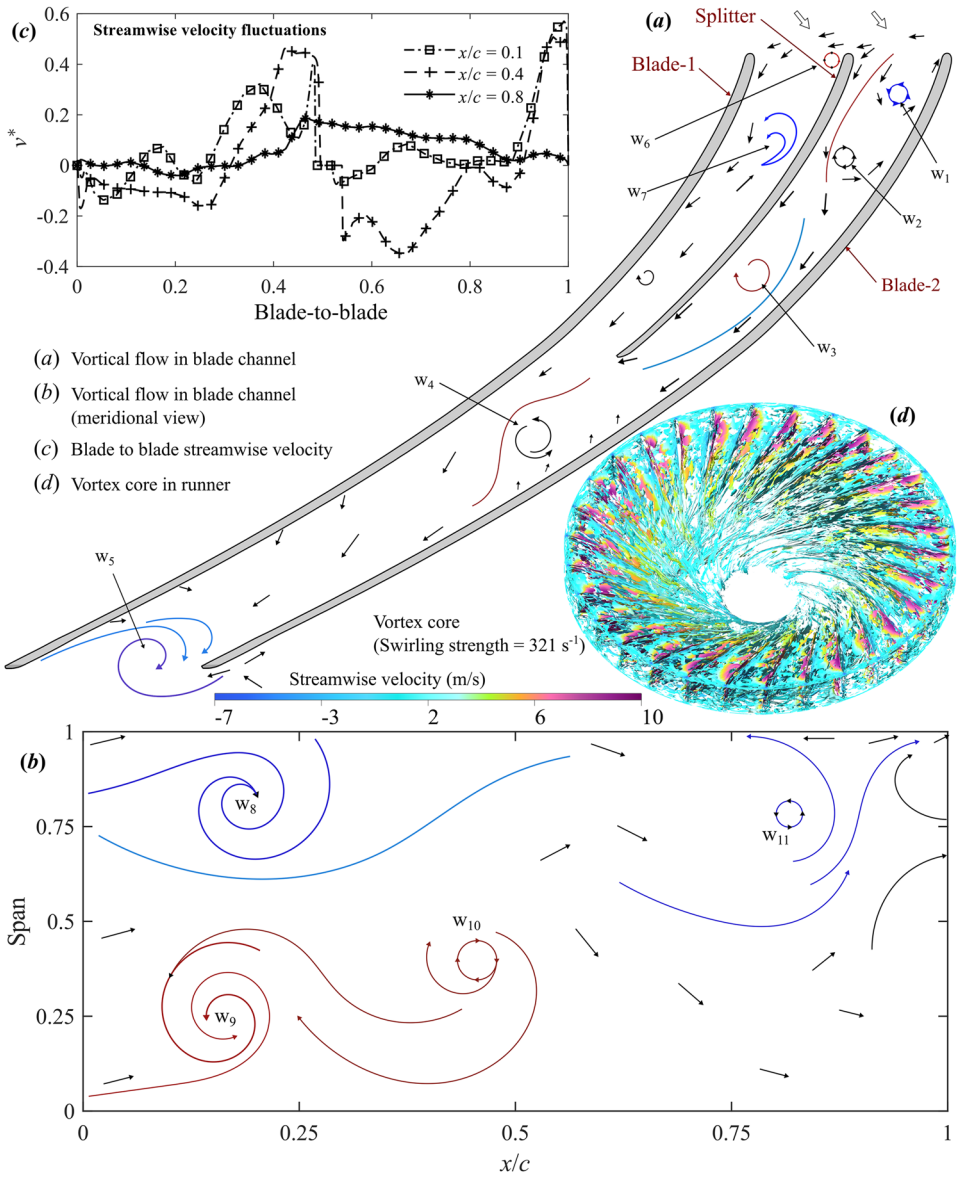

FIG. 10. Inception of vortical flow (time-average) in the blade channel, velocity fluctuations, and swirling strength. (a) shows distinct positions of swirling regions in the channel; the vortical pattern is established by averaging over five revolutions of the runner. (b) shows the meridional view of the vortical structure in the middle of the blade channel, i.e., between the splitter and blade–1 from x/c = 0–0.5 and between blade–1 and blade–2 from x/c = 0.5 to 1. (c) shows the streamwise velocity fluctuations in the mid-span of one of the blade channels at x/c = 0.1, 0.4, and 0.8; the blade-to-blade value of zero indicates the pressure-side of blade–2, and the value of one indicates the suction-side of blade–1. (d) shows the vortex core by the swirling strength of 321 s^{-1} in the runner, and the color represents the time-averaged streamwise velocity.

of the runner. Blade-to-blade values of zero and one represent the pressure- (blade–2) and suction-sides (blade–1) of the blade channel, respectively. The influence of vortices can be seen on the streamwise velocity. For example, velocity along x/c = 0.4 shows negative velocity around the blade-to-blade distance of 0.6, which is due to vortex w_3. The positive velocity represents the sound (accelerating) flow near the blade–1 suction-side (region w_7). A visualization of the turbulent structure in the runner is presented in Fig. 10(d). Swirling strength, which identifies the vortex structure based on imaginary eigenvalues of the velocity gradient ($\nabla \mathbf{u}$) with quantification of swirling strength in the vortex, is not an exact measure of vortex breakdown.[55] The swirling strength of the vortex core is 321 s^{-1}, and the vortex core is colored by time-average streamwise velocity, which shows the regions of accelerating and decelerating flow in the blade channels. Positive streamwise velocity indicates normal flow, and the negative velocity indicates reverse flow, which gives momentum to the vortex rings.

Vorticity contours in the blade cascade at time instants of (a) 6°, (b) 12°, (c) 18°, and (d) 24° different angular positions of the runner are shown in Fig. 11. Blade passage from the runner inlet to the splitter trailing edge is shown, and three channels of the blade cascade (96°) are monitored. As the runner (blade) rotates, relative to the guide vane, the vortex position and strength change in the cascade. Flow separation from the blade leading edge, toward the suction-side, leads to formation of a vortical region at the inlet. The vortical region grows and interacts with other regions and further breaks down. The temporal inception of the vortex rings in the blade channel is investigated and presented in Fig. 12. Figure 12 is prepared by overlapping the streamline data at the mid-span of the runner for each revolution, and the five revolutions of the runner are considered. The angular movement of one blade channel—as shown in Fig. 10(a)—was traced from 0° to 24°. Then, the length (x/c) and width (s) of the blade channel were normalized between 0 and 1, and the predominant streamlines are extracted. The pitch (s) shows the blade-to-blade distance starting from the suction-side of blade–1 (s = 0) to the pressure-side of blade–2 (s = 1); the value of 0.5 indicates the splitter. Figures 12(a)–12(l) show the vortical structure of vortex rings when the angular position (θ) of the blade channels is 0°, 2°, 4°, 6°, 8°, 10°, 12°, 14°, 16°, 18°, 20°, and 22°, respectively. The right-hand rule is used to explain spatial coordinates and the axis of rotation in this figure. The runner rotates in the negative direction. At the reference position (θ = 0°), vortical regions w_1, w_2, and w_7 are clearly visible, where w_1 rotates in the positive direction, w_2 rotates in the negative direction, and w_7 rotates in the positive direction. As the blade advances from 0° to 2°, vortical region w_3 is established on the pressure-side of blade–2 (x/c = 0.4) and interacts with w_2. Vortical region w_7 is developed further, and the size increases as the blade advances. At θ = 4° position, the formation of vortical region w_4 begins at the splitter trailing edge. The formation is the result of the splitting of the w_2 and w_3 regions as well as the accelerating flow from the splitter pressure-side. At θ = 6° position, interestingly, four vortical regions appear between the splitter suction-side and blade–2 pressure-side. Region w_2 splits again into two parts and forms a large region of a

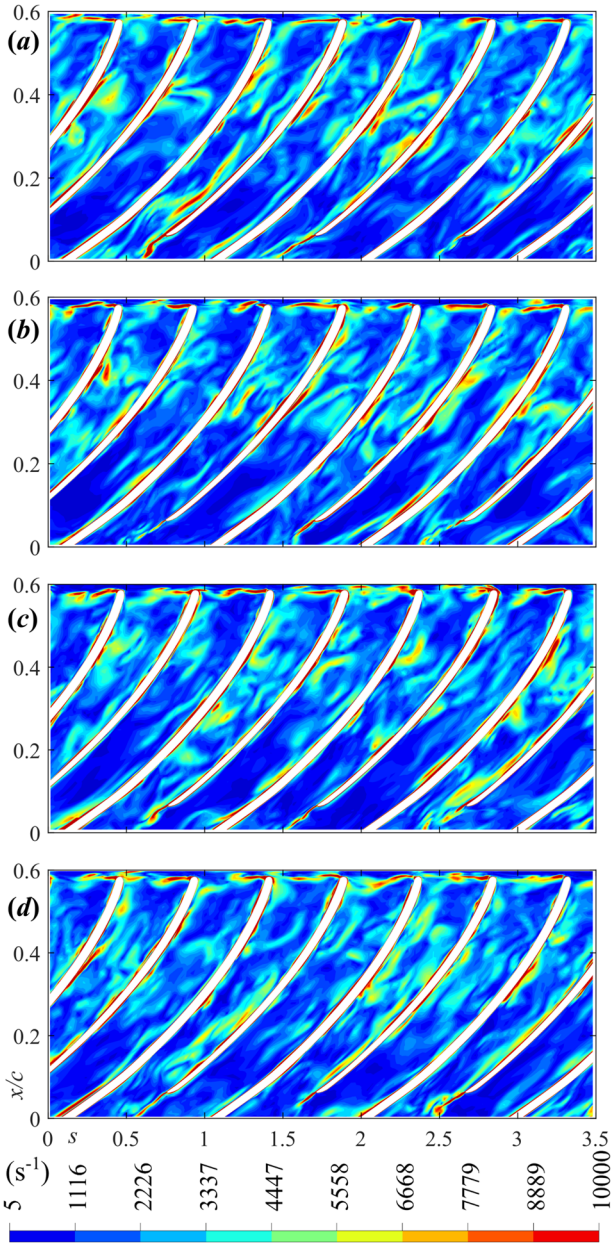

FIG. 11. Vorticity contours in the blade cascade at time instants of (a) 6°, (b) 12°, (c) 18°, and (d) 24° different angular positions of the runner; x/c = 0–1 shows the dimensionless distance from the blade leading edge to the trailing edge.

perfect vortex ring, which is axially extended up to the crown [1%–75% span, shown in Fig. 9(a)]. Full development of the vortical regions can be seen at θ = 10°, where the flow blockade (stall) between the splitter suction-side and the pressure-side of blade–2 is more than 90%. A new vortical region, w_{12}, is established on the pressure-side of blade–2 (x/c = 0.6) at θ = 12°, which rotates in the positive direction. The rotational direction is strongly affected by the reverse (pumping) flow attached to the blade pressure-side. Later, at θ = 14°, this vortical region constitutes a scroll and moves toward the splitter trailing edge. Vortical region w_1 again grows rapidly, which can be seen for 16°, 18°, and 20° positions. The w_1 region blocks the flow entering into the blade cascade and keeps rotating in the positive direction. Due to this blockade, flow quickly decelerates

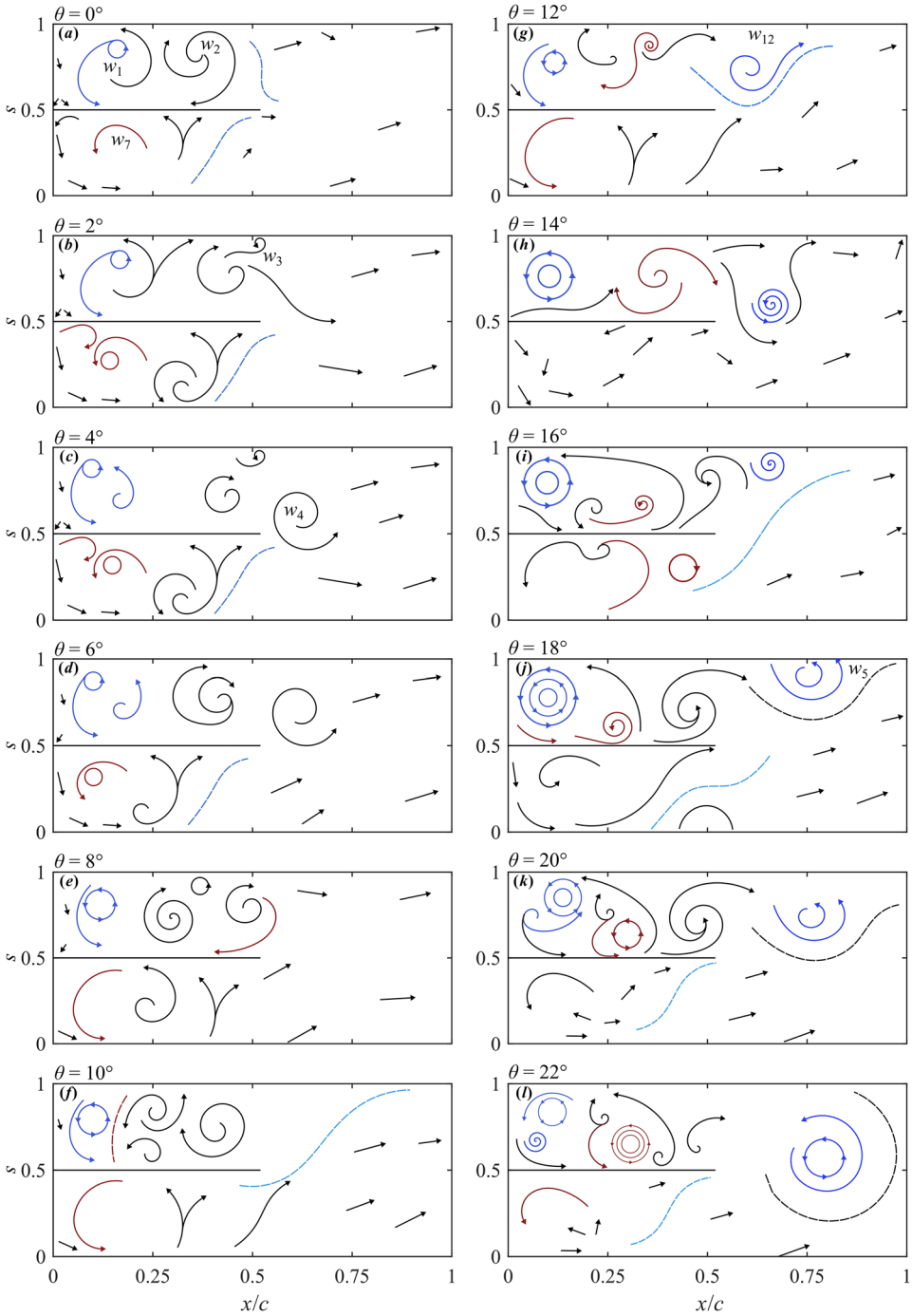

FIG. 12. The trajectory and inception of vortex rings in one of the blade channels; pitch (s) on the y-axis is the normalized blade-to-blade distance from the suction-side of blade–1 to the pressure-side of blade–2; the straight line at $s = 0.5$ on the y-axis indicates the splitter; $x/c = 0$–1 shows the dimensionless distance from the blade leading edge to the trailing edge. [(a)–(l)] show the vortical structure of the vortex rings when the angular position (θ) of the blade channels is 0°, 2°, 4°, 6°, 8°, 10°, 12°, 14°, 16°, 18°, 20°, and 22°, respectively.

on the pressure-side of blade–2 from $x/c = 0.95$ and $x/c = 0.6$ and accelerates on the suction-side of blade–1 from $x/c = 0.6$ and $x/c = 0.95$ in the channel. Consequently, vortical region w_5 gains momentum and becomes larger (see at $\theta = 22°$). This region creates a blockade at the channel outlet, and the entire blade passage experiences stalls for the moment.

C. Interaction between vortex rings and large vortex street

Vortical flow leaving the blade cascade enters the draft tube, where an adverse pressure gradient is dominant. Two pressure sensors (D_1 and D_2) were integrated into the draft tube to investigate stochastic and deterministic frequencies. Figure 13(a) shows the frequency spectra at the D_1 location. The spectral analysis revealed both frequencies at high amplitudes. The deterministic frequency corresponded to the runner angular speed (n_R) and the blade passing frequency (f_b) at both locations in the draft tube. However, the amplitudes are very small compared to the amplitudes obtained in vaneless space. The amplitudes are similar to those of the stochastic frequencies of 10–200 Hz. The compressible LES shows good agreement with the experimental data for both deterministic and stochastic frequencies. This approach is allowed to resolve high-frequency spectra, where the special interest is stochastic fluctuations around the blade passing frequency. As discussed in the Introduction, such high-frequency fluctuations cause cyclic fatigue, especially around trailing edge junctions to the crown and the band. Moreover, the vortex ring

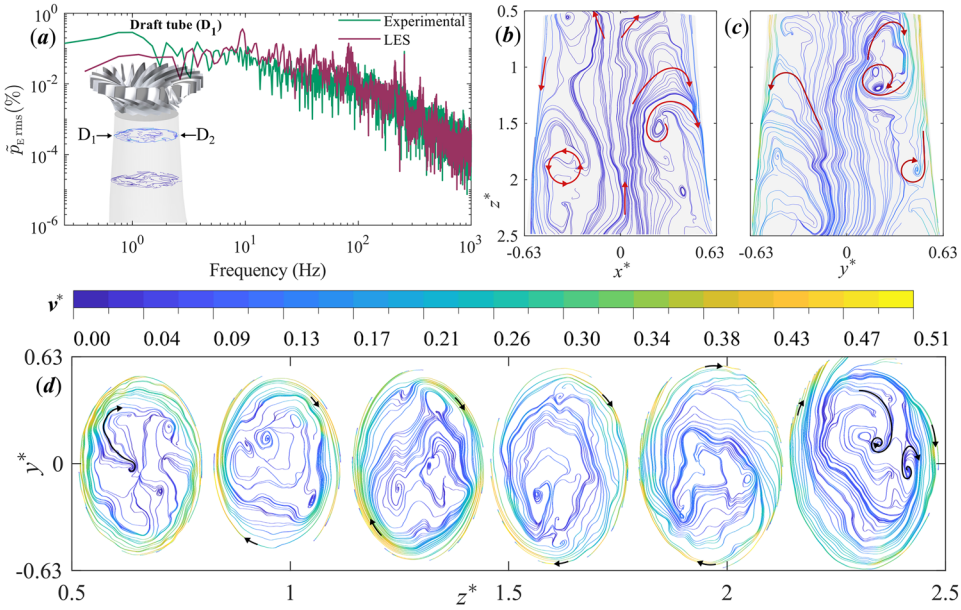

FIG. 13. Frequency spectra of unsteady pressure fluctuations in the draft tube (location–D_1) and vortex rings (streamlines colored by velocity) in the draft tube. (a) Frequency of unsteady pressure fluctuations at the D_1 location and comparison with the LES. [(b) and (c)] Streamlines in the draft tube cone at the mid-plane in the axial direction. The streamlines are colored by dimensionless velocity (v^*). (d) Streamlines on the slicing plane from the runner outlet to the draft tube elbow, the streamlines are colored by dimensionless velocity (v^*). Dimensionless axes x^*, y^*, and z^* are normalized by the characteristic length (L_c), i.e., runner reference diameter of 349 mm.

located at the blade trailing edge interacts with the recirculating (pumping) flow from the draft tube core, and induces high frequency fluctuations. Figures 13(b) and 13(c) show streamlines of velocity on the axial plane (z-direction) along the x- and y-directions. A dimensionless axial distance (z^*) of 0.5 and 2.5 indicates the locations of the runner outlet and the elbow (start of inner radius), respectively. The streamlines are colored by velocity (v^*) using Eq. (8). The streamlines clearly show the strong presence of vortical flow in the draft tube. More interestingly, flow in the center core is pumping upward, i.e., runner. Flow near the draft tube wall is accelerating downward, i.e., elbow. Separated flow from the draft tube wall, due to an adverse pressure gradient, interacts with the core and starts forming vortex rings. Strong flow separation takes place near the runner band as the cross-sectional area increases in the flow direction (i.e., toward the draft tube). The boundary layer is almost broken, and the flow detaches from the wall of the runner band and, consequently, the adverse gradient of pressure becomes predominant. The other important factor is complete breakdown of the boundary layer at the junction of the runner and the draft tube due to the jet-type flow from the labyrinth (band) seal. Consequently, the shear layer between the viscous and turbulent layers collapses, and the adverse pressure gradient again sets on in the draft tube. A distinct pattern of recirculating flow is obtained between the runner outlet and the elbow. For example, flow in the core region is directed toward the runner center, known as the cone, which interacts with the blockade region w_5 (see Fig. 10) at the blade trailing edge. When the blade channel blockade opens, mainly w_2, w_4, w_5, and w_{12} regions, the pumping flow from the draft tube is quickly pushed toward the band due to high centrifugal force. Then, flow returns from the runner outlet. At a distance of approximately $z^* = 1.5$, the vortical structure is established along the circumference. Figures 13(b) and 13(c) show vortex rings along the x- and y-directions, and Fig. 13(d) shows vortex rings along the axial directions at different slicing planes. The slices at $z^* = 0.5$, 0.9, and 2.3 represent the locations at the runner outlet, sensor D_1, and before the elbow, respectively. The figure shows how vortex rings change their shape in the axial direction. The vortex rings, which rotate opposite to the runner rotation, gain momentum from the pumping flow returned from the elbow and separating flow from the wall. The rings near the draft tube wall have a rotational direction similar to the runner; however, rings located in the core region rotate opposite to the runner rotation. The source of high amplitude stochastic pressure fluctuations is the vortex rings and the temporal change of their locations, which is synchronized with the flow blockade between the splitter and the blade, the blade channel outlet, and the draft tube elbow. Reverse flow, especially pumping, also contributes significantly to develop high-amplitude stochastic fluctuations in the blade channel. Due to the high centrifugal force associated with the high rotational speed of the runner, the rings continuously change their location in both radial and spanwise directions in the runner. The spatial position of the vortex rings continuously changes, which is dependent on the blockade in the draft tube elbow.

Overall, wake from the guide vanes and interactions with the blade stagnation point change the flow structure in the blade channel, driving flow separation from the blade suction-side and vortex rings, w_1 and w_2. However, reverse flow on the blade pressure-side near the runner crown and band causes a blockade in the channel. Consequently, pressure amplitudes increase quickly. Similarly, flow at the runner outlet is influenced by the settling pattern of the scroll rings in the axial direction and the blockage in the draft tube elbow. High circumferential velocity and the centrifugal force push the vortex rings from one side of the blade to another and from the crown to the band continuously.

IV. CONCLUSIONS

The present study allowed us to understand the complex mechanism of temporal inception of vortical rings in the blade cascade, as well as how these rings interact with each other and dissipate energy to the blades. One of the

dangerous operating conditions of a turbine was investigated, where the circumferential velocity was two times the design condition. Eight sensors at distinct locations revealed important details on the inception of vortical flow and the interaction with secondary flow in the vaneless space, blade cascade, and draft tube. To establish the credibility of the measured data and verify the repeatability, detailed calibration and uncertainty quantification of all the sensors were conducted before the present measurements. Compressible large eddy simulations were performed to investigate the formation and the inception of the rings. The computational domain consisted of 72×10^6 nodes of hexahedral elements. A verification technique known as the index of resolution quality for large eddy simulations, in addition to Pope's criterion, was used, and more than 80% of the turbulent spectrum was resolved.

Investigations on wake inception behind a guide vane showed that the size of the blade stagnation point changes significantly when it passes by the wake of the guide vane. The size of the stagnation point is minimal when a blade interacts with the guide vane trailing edge. The size increases quickly as the blade advances and attains a maximum when the blade is exactly between two guide vanes, i.e., $\theta = 6°$. Furthermore, the interaction between the wake and the stagnation point strongly affected the flow separation in the blade cascade. This separated flow induces a secondary flow in the blade channel and gives momentum to the vortex rings. The rings attached to the blade suction-side rotate in the positive direction, and the rings that gain momentum from the reverse flow on the blade pressure-side rotate in the negative direction, i.e., similar to the runner rotation. The vortex rings interact with the secondary flow in the channels, and the size of the ring increases due to the merging of the two small rings. When the ring size equals the width of the channel, the ring size blocks the channel and dissipates high energy to the blades. In fact, such a blockade occurs at two distinct locations in the blade channel, and both regions contribute to increase the intensity of the fluctuating pressure in the entire channel. A vortex ring located at the blade trailing edge gains momentum from the pumping flow originating in the draft tube core, which pushes the entire blockade toward the runner band due to high centrifugal force. High circumferential velocity forces the blockade region to remain attached near the blade trailing edge junction to the band. Reverse flow in the core region forms vortex rings when it interacts with the secondary flow originating from the adverse pressure gradient of the draft tube wall. The reverse flow from the runner outlet to the draft tube elbow is driven by two vortical regions concentrated in the elbow. Both vortical regions rotate in opposite directions, where one region (located at the inner radius of the elbow) tries to push the flow toward the runner, whereas the other region (located at the outer radius of the elbow) tries to push the flow toward the outlet.

ACKNOWLEDGMENTS

The experimental and numerical studies were conducted under the research project HiFrancis—High Head Francis Turbine. The project (No. 254987) was financed by The Research Council of Norway and the Norwegian hydropower industries. The authors would also like to acknowledge the Vilje supercomputer (www.hpc.ntnu.no) at NTNU for providing necessary resources to carry out the large simulations.

NOMENCLATURE

Abbreviations

BEP	best efficiency point
LES	large eddy simulation
RANS	Reynolds-averaged Navier-Stokes
RSI	rotor-stator interaction
SAS	scale-adaptive simulation
SGS	sub-grid scale
WALE	wall-adapted local eddy-viscosity

Variables

a	speed of sound (m s^{-1})
C_a	acoustic Courant number
c	blade/guide vane chord (m)
D	diameter (m)
E	specific hydraulic energy (J kg^{-1}); $E = g \times H$
$\hat{e}$	error/uncertainty
f	frequency (Hz)
g	gravity (m s^{-2}); $g = 9.821\,465$ m s^{-2}
H	head (m)
K	bulk viscosity of water (Pa)
L_c	thickness (m), characteristic length (m)
n	runner angular speed (revolution per second)
n_{ED}	speed factor
p	pressure (Pa)
$\tilde{p}_E$	factor of pressure fluctuations
Q	discharge (m^3 s^{-1})
Q_{ED}	discharge factor
s	pitch (deg), blade-to-blade distance
T	torque (N m)
t	time (s)
v	velocity (m s^{-1})
y^+	dimensionless node spacing
z	number of blades/guide vanes

Greek letters

θ	runner angular position (deg)
ρ	water density (kg m^{-3})
ω	angular speed (rad/s)
ν	kinematic viscosity (m^{-2} s^{-1})
η_h	hydraulic efficiency

Subscripts

a	axial
b	blade
c	characteristic
gv	guide vane
R	runaway
r	random, radial
rms	root-mean-square

s	systematic
st	streamwise
t	total
ω	circumferential

Dimensionless number

Eu	Euler number, Eu = $g \times H/(\omega^2 \times D^2)$
Fr	Froude number, Fr = $\omega\sqrt{D/g}$
Re	Reynolds number, Re = $\omega \times D^2/2\nu$
St	Strouhal number, St = $\omega \times D^3/Q$

APPENDIX: MESH RESOLUTION AND UNCERTAINTY QUANTIFICATION

1. Grid convergence index

The mesh independence study was carried out to determine the numerical uncertainty in the computational domain. Simulations of the mesh independence study were performed considering steady compressible flow. Mesh–m_1 is the coarse mesh with 9×10^6 nodes, and mesh–m_4 is the fine mesh with 72×10^6 nodes. An average cell size of fine mesh is 0.97 mm. The mesh quality, including the aspect ratio, orthogonality, and expansion factor were 0.45, 0.4, and 0.5, respectively. The element quality matrix varied between zero (poor quality) and one (best quality). The grid-convergence-index (GCI), proposed by Celik *et al.*,[45] was used to determine the error in mesh discretization,

$$\hat{e}_{\text{fine}} = \frac{1.25 e_{\text{apr(r)}}}{r^k - 1}, \tag{A1}$$

where $e_{\text{apr(r)}}$ is the approximate relative error, r is the mesh refinement ratio ($r \cong 2$), and k is the apparent order. Computed errors ($\hat{e}_{\text{GCI}}$) in pressure values at locations V_1, R_1, and r_4 are 0.3%, 0.41%, and 0.5%, respectively. The large error at the R_4 location in the runner is attributed to flow separation and swirling, where the steady-state SST model was unable to predict pressure loading accurately.

2. Index of resolution quality

Large eddy simulations specifically require proper verification since they rely on unsteady resolved motion in the cells to drive large-scale turbulent transport. The formation process of the large eddies must be captured with sufficient fidelity to ensure that the statistics of turbulence are accurate, and the filter width must be small enough to minimize the influence of the modeled part. A verification technique, the index of resolution quality for large eddy simulations (LES_IQ), proposed by Celik *et al.*,[46] is widely used to evaluate the quality of the resolved turbulent spectrum. The LES_IQ is the ratio of resolved turbulent kinetic energy k_{resolved} to total turbulent kinetic energy k_{total},

$$\hat{e}_{\text{LES\_IQ}} = \frac{k_{\text{resolved}}}{k_{\text{total}}} = \frac{k_{\text{resolved}}}{k_{\text{resolved}} + a_k h^p}, \tag{A2}$$

where h is an average cell size, p is the order of accuracy of the numerical scheme, and a_k is the coefficient, which can be determined as

$$a_k = \frac{1}{h_2^p}\left[\frac{k_2^{\text{resolved}} - k_1^{\text{resolved}}}{r^p - 1}\right], \tag{A3}$$

where r is the mesh refinement ratio ($r > 1$) and subscripts (1) and (2) denote the quantities obtained on mesh (1) and mesh (2), respectively,

$$k_{\text{resolved}} = 0.5\left((u - \bar{u})^2 + (v - \bar{v})^2 + (w - \bar{w})^2\right)\ (\text{m}^2\ \text{s}^{-2}), \tag{A4}$$

where u, v, and w are the velocity components. Celik *et al.*[46] suggested that an LES_IQ of 75% to 85% can be considered adequate for high-Reynolds-number flow. The computed LES_IQ ranges from 70% to 85% in the turbine for the present study with 72×10^6 nodes. Figure 14 shows the turbulent structure of the Q-criterion in the runner with the fine mesh,

$$Q = C_q\left(\Omega^2 - S^2\right)\ (\text{s}^{-2}), \tag{A5}$$

where $C_q = 0.25$, S is the absolute value of the strain rate, $S = \sqrt{2S_{ij}S_{ij}}$, $S_{ij} = \frac{1}{2}(\frac{\partial U_i}{\partial x_j} + \frac{\partial U_j}{\partial x_i})$, Ω is the absolute value of the vorticity, $\Omega = \sqrt{2\omega_{ij}\omega_{ij}}$, and $\omega_{ij} = \frac{1}{2}(\frac{\partial U_i}{\partial x_j} - \frac{\partial U_j}{\partial x_i})$.[56] The value of Q is 6830 s^{-2} for the prepared iso-surface in the figure, and the contours show the velocity in the runner. Flow unsteadiness and different sizes of turbulent structures in the blade channels can be seen clearly. From the measurements, high amplitude stochastic pressure fluctuations were observed in the blade passage. From the iso-surface of the Q-criterion, the stochastic fluctuations are evidently associated with vortical turbulent flow.

3. Pope's criterion (M)

Another technique called "Pope's criterion (M)" was used to estimate the resolved and modeled turbulent spectrum in the runner. According to Pope's recommendation, the resolved turbulent kinetic energy should be above 80% of the total kinetic energy,

$$\hat{e}_{\text{M}} = 1 - \frac{k_{\text{sgs}}}{k_{\text{sgs}} + k_{\text{resolved}}}, \tag{A6}$$

where k_{sgs} is the modeled turbulent spectrum by the SGS filter in the LES. Figure 15 shows that most of the turbulent

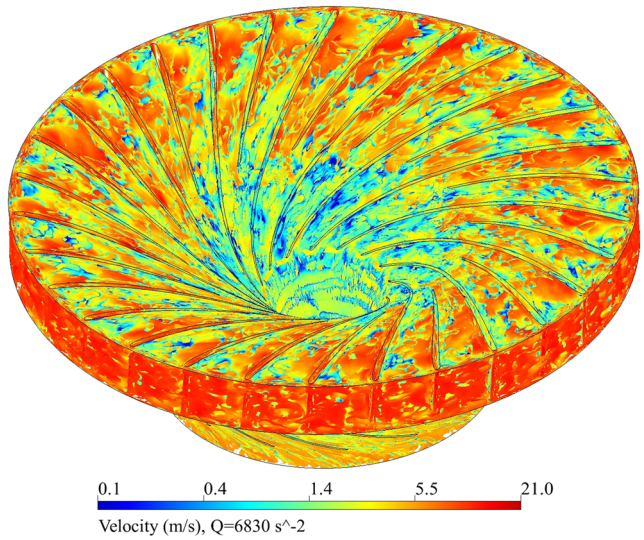

FIG. 14. Turbulent structures in the runner iso-surface of Q [=Cq(Ω^2 – S^2)], where $Q = 6830\ \text{s}^{-2}$. The color indicates the velocity in the runner.

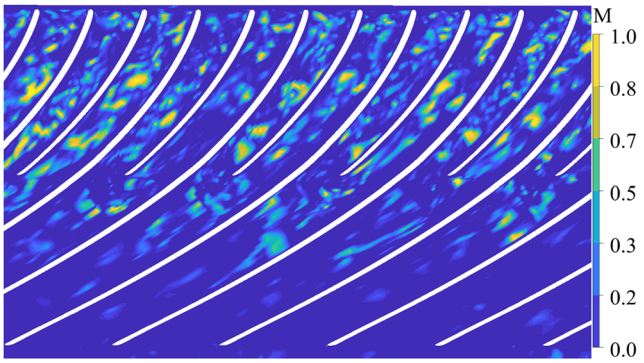

FIG. 15. Pope's criterion (M) on resolved and modeled turbulent kinetic energy in the runner (mid-span). M = 0 is equivalent to DNS, and M = 1 is equivalent to the RANS solution.

spectrum is resolved in the runner. More than 80% of the spectrum has $M \geq 0.2$, except a few locations where $0.3 \leq M \leq 1$. However, these locations are changing with runner rotation and are dependent on the instantaneous position of the runner.

[1]H. Honji, "Streaked flow around an oscillating circular cylinder," J. Fluid Mech. **107**, 509 (1981).
[2]B. T. Tan, K. Y. S. Liow, L. Mununga, M. C. Thompson, and K. Hourigan, "Simulation of the control of vortex breakdown in a closed cylinder using a small rotating disk," Phys. Fluids **21**, 024104 (2009).
[3]T. Sarpkaya, "On stationary and travelling vortex breakdowns," J. Fluid Mech. **45**, 545 (1971).
[4]M. G. Hall, "Vortex breakdown," Annu. Rev. Fluid. Mech. **4**, 195 (1972).
[5]A. Ducoin, J. A. Astolfi, F. Deniset, and J.-F. Sigrist, "Computational and experimental investigation of flow over a transient pitching hydrofoil," Eur. J. Mech.- B/Fluids **28**, 728 (2009).
[6]B. Di Pierro and M. Abid, "Energy spectra in a helical vortex breakdown," Phys. Fluids **23**, 025104 (2011).
[7]A. Ducoin, J. A. Astolfi, and J.-F. Sigrist, "An experimental analysis of fluid structure interaction on a flexible hydrofoil in various flow regimes including cavitating flow," Eur. J. Mech.- B/Fluids **36**, 63 (2012).
[8]A. Ducoin, J. C. Loiseau, and J. C. Robinet, "Numerical investigation of the interaction between laminar to turbulent transition and the wake of an airfoil," Eur. J. Mech.- B/Fluids **57**, 231 (2016).
[9]D. Bourgoyne, J. Hamel, S. Ceccio, and D. Dowling, "Time-averaged flow over a hydrofoil at high Reynolds number," J. Fluid Mech. **496**, 365 (2003).
[10]D. A. Bourgoyne, S. L. Ceccio, and D. R. Dowling, "Vortex shedding from a hydrofoil at high Reynolds number," J. Fluid Mech. **531**, 293 (2005).
[11]S. Pasche, F. Gallaire, and F. Avellan, "Predictive control of spiral vortex breakdown," J. Fluid Mech. **842**, 58 (2018).
[12]R. Goyal, B. K. Gandhi, and M. J. Cervantes, "Experimental study of mitigation of a spiral vortex breakdown at high Reynolds number under an adverse pressure gradient," Phys. Fluids **29**, 104104 (2017).
[13]C. Trivedi, B. K. Gandhi, and M. J. Cervantes, "Effect of transients on Francis turbine runner life: A review," J. Hydraul. Res. **51**, 121 (2013).
[14]X. Liu, Y. Luo, and Z. Wang, "A review on fatigue damage mechanism in hydro turbines," Renewable Sustainable Energy Rev. **54**, 1 (2016).
[15]C. Trivedi and M. J. Cervantes, "Fluid structure interaction in hydraulic turbines: A perspective review," Renewable Sustainable Energy Rev. **68**, 87 (2017).
[16]H. Ohashi, "Case study of pump failure due to rotor-stator interaction," Int. J. Rotating Mach. **1**, 53 (1994).
[17]U. Dorji and R. Ghomashchi, "Hydro turbine failure mechanisms: An overview," Eng. Failure Anal. **44**, 136 (2014).
[18]A. Luna-Ramírez, A. Campos-Amezcua, O. Dorantes-Gómez, Z. Mazur-Czerwiec, and R. Muñoz-Quezada, "Failure analysis of runner blades in a Francis hydraulic turbine—Case study," Eng. Failure Anal. **59**, 314 (2016).
[19]Z. Zuo, S. Liu, Y. Sun, and Y. Wu, "Pressure fluctuations in the vaneless space of high-head pump-turbines—A review," Renewable Sustainable Energy Rev. **41**, 965 (2015).
[20]C. Trivedi, M. Cervantes, B. Gandhi, and O. Dahlhaug, "Transient pressure measurements on a high head model Francis turbine during emergency shutdown, total load rejection, and runaway," J. Fluids Eng. **136**, 121107 (2014).
[21]C. Trivedi, M. J. Cervantes, and B. K. Gandhi, "Numerical investigation and validation of a Francis turbine at runaway operating conditions," Energies **9**, 22 (2016).
[22]X. Zhang, Y. Cheng, L. Xia, J. Yang, and Z. Qian, "Looping dynamic characteristics of a pump-turbine in the S-shaped region during runaway," J. Fluids Eng. **138**, 091102 (2016).
[23]W. Zeng, J. Yang, and W. Guo, "Runaway instability of pump-turbines in S-shaped regions considering water compressibility," J. Fluids Eng. **137**, 051401 (2015).
[24]W. Zeng, J. Yang, J. Hu, and J. Yang, "Guide-vane closing schemes for pump-turbines based on transient characteristics in S-shaped region," J. Fluids Eng. **138**, 051302 (2016).
[25]L. Xia, Y. Cheng, Z. Yang, J. You, J. Yang, and Z. Qian, "Evolutions of pressure fluctuations and runner loads during runaway processes of a pump-turbine," J. Fluids Eng. **139**, 091101 (2017).
[26]V. Hasmatuchi, M. Farhat, S. Roth, F. Botero, and F. Avellan, "Experimental evidence of rotating stall in a pump-turbine at off-design conditions in generating mode," J. Fluids Eng. **133**, 051104 (2011).
[27]F. Botero, V. Hasmatuchi, S. Roth, and M. Farhat, "Non-intrusive detection of rotating stall in pump-turbines," Mech. Syst. Signal Process. **48**, 162 (2014).
[28]A. Rezghi and A. Riasi, "Sensitivity analysis of transient flow of two parallel pump-turbines operating at runaway," Renewable Energy **86**, 611 (2016).
[29]M. Xiuli, P. Giorgio, and Z. Yuan, "Francis-type reversible turbine field investigation during fast closure of wicket gates," J. Fluids Eng. **140**, 061103 (2018).
[30]F. R. Menter and Y. Egorov, in *Direct Large-Eddy Simulation VI*, edited by E. Lamballais, R. Friedrich, B. Geurts, and O. Métais (Springer, The Netherlands, 2006), pp. 687–694.
[31]C. Mende, W. Weber, and U. Seidel, "Progress in load prediction for speed-no-load operation in Francis turbines," IOP Conf. Ser.: Earth Environ. Sci. **49**, 062017 (2016).
[32]M. Younsi, A. Djerrada, T. Belamri, and F. Menter, "Application of the SAS turbulence model to predict the unsteady flow field behaviour in a forward centrifugal fan," Int. J. Comput. Fluid Dyn. **22**, 639 (2008).
[33]P. Olivier, K. Chisachi, and A. François, "High-resolution LES of the rotating stall in a reduced scale model pump-turbine," IOP Conf. Ser.: Earth Environ. Sci. **22**, 022018 (2014).
[34]O. Pacot, C. Kato, Y. Guo, Y. Yamade, and F. Avellan, "Large eddy simulation of the rotating stall in a pump-turbine operated in pumping mode at a part-load condition," J. Fluids Eng. **138**, 111102 (2016).
[35]C. Trivedi, "Compressible large eddy simulation of a Francis turbine during speed-no-load: Rotor stator interaction and inception of a vortical flow," J. Eng. Gas Turbines Power **140**, 112601 (2018).
[36]C. Widmer, T. Staubli, and N. Ledergerber, "Unstable characteristics and rotating stall in turbine brake operation of pump-turbines," J. Fluids Eng. **133**, 041101 (2011).
[37]J. L. Xiao, E. Q. Zhu, and G. D. Wang, "Numerical simulation of emergency shutdown process of ring gate in hydraulic turbine runaway," J. Fluids Eng. **134**, 124501 (2012).
[38]L. S. Xia, Y. G. Cheng, X. X. Zhang, and J. D. Yang, "Numerical analysis of rotating stall instabilities of a pump-turbine in pump mode," IOP Conf. Ser.: Earth Environ. Sci. **22**, 032020 (2014).
[39]M. Fortin, S. Houde, and C. Deschenes, "Validation of simulation strategies for the flow in a model propeller turbine during a runaway event," IOP Conf. Ser.: Earth Environ. Sci. **22**, 032026 (2014).
[40]C. Trivedi, M. J. Cervantes, and O. G. Dahlhaug, "Numerical techniques applied to hydraulic turbines: A perspective review," Appl. Mech. Rev. **68**, 29 (2016).
[41]C. Trivedi, "Investigations of compressible turbulent flow in a high head Francis turbine," J. Fluids Eng. **140**, 011101 (2018).
[42]J. Yan, J. Koutnik, U. Seidel, and B. Huebner, "Compressible simulation of rotor-stator interaction in pump-turbines," IOP Conf. Ser.: Earth Environ. Sci. **12**, 012008 (2010).
[43]IEC 60193, Hydraulic Turbines, Storage Pumps and Pump-Turbines: Model Acceptance Tests, International Electrotechnical Commission, 3, Rue de Varembé, PO Box 131, CH-1211 Geneva 20, Switzerland, 16 November, 1999, p. 578.
[44]J. Yin, D. Wang, L. Wang, Y. Wu, and X. Wei, "Effects of water compressibility on the pressure fluctuation prediction in pump turbine," IOP Conf. Ser.: Earth Environ. Sci. **15**, 062030 (2012).

[45]I. B. Celik, U. Ghia, P. J. Roache, and C. J. Freitas, "Procedure for estimation and reporting of uncertainty due to discretization in CFD applications," J. Fluids Eng. **130**, 4 (2008).
[46]I. B. Celik, Z. N. Cehreli, and I. Yavuz, "Index of resolution quality for large eddy simulations," J. Fluids Eng. **127**, 949 (2005).
[47]S. B. Pope, "Ten questions concerning the large-eddy simulation of turbulent flows," New J. Phys. **6**, 35 (2004).
[48]M. Shur, P. R. Spalart, M. Strelets, and A. Travin, "A rapid and accurate switch from RANS to LES in boundary layers using an overlap region," Flow, Turbul. Combust. **86**, 179 (2011).
[49]C. Mockett, M. Fuchs, and F. Thiele, "Progress in DES for wall-modelled LES of complex internal flows," Comput. Fluids **65**, 44 (2012).
[50]A. A. Gavrilov, A. V. Sentyabov, A. A. Dekterev, and K. Hanjalić, "Vortical structures and pressure pulsations in draft tube of a Francis-99 turbine at part load: RANS and hybrid RANS/LES analysis," Int. J. Heat Fluid Flow **63**, 158 (2017).
[51]N. V. Nikitin, F. Nicoud, B. Wasistho, K. D. Squires, and P. R. Spalart, "An approach to wall modeling in large-eddy simulations," Phys. Fluids **12**, 1629 (2000).
[52]E. Garnier, N. Adams, and P. Sagaut, *Large Eddy Simulation for Compressible Flows, First* (Springer, The Netherlands, 2009).
[53]IEC 60193, Hydraulic Turbines, Storage Pumps and Pump-Turbines: Model Acceptance Tests, International Electrotechnical Commission, 3, Rue de Varembé, PO Box 131, CH-1211 Geneva 20, Switzerland, 16 November, 1999, p. 569.
[54]H. Brekke, *New Trends in Technologies: Devices, Computer, Communication and Industrial Systems* (InTech, Rijeka, Croatia, 2010), pp. 217–232.
[55]V. Kolar, "Vortex identification: New requirements and limitations," Int. J. Heat Fluid Flow **28**, 638 (2007).
[56]Y. Dubief and F. Delcayre, "On coherent-vortex identification in turbulence," J. Turbul. **1**, 1 (2000).